Short-pulse laser harmonics from oscillating plasma surfaces driven at relativistic intensity

R. Lichters, J. Meyer-ter-Vehn and A. Pukhov

View Online   Export Citation

ARTICLES YOU MAY BE INTERESTED IN

Short-pulse laser harmonics from oscillating plasma surfaces driven at relativistic intensity

R. Lichters, J. Meyer-ter-Vehn, and A. Pukhov
Max-Planck-Institut für Quantenoptik, Hans-Kopfermann-Str. 1, 85748 Garching, Germany

The generation of harmonics by interaction of an ultrashort laser pulse with a step boundary of a plane overdense plasma layer is studied at intensities $I\lambda^2 = 10^{17} - 10^{19}$ W cm^{-2} μm^2 for normal and oblique incidence and different polarizations. Fully relativistic one-dimensional particle-in-cell (PIC) simulations are performed with high spectral resolution. Harmonic emission increases with intensity and also when lowering the plasma density. The simulations reveal strong oscillations of the critical surface driven by the normal component of the laser field and by the ponderomotive force. It is shown that the generation of harmonics can be understood as reflection from the oscillating surface, taking full account of retardation. Describing the oscillations by one or more Fourier components with adjustable amplitudes, model spectra are obtained that well reproduce the PIC spectra. The model is based on relativistic cold plasma equations for oblique incidence. General selection rules concerning polarization of odd and even harmonics depending on incident polarization are derived. © *1996 American Institute of Physics.* [S1070-664X(96)04009-8]

I. INTRODUCTION

Recent progress in making ultrashort (10–100 fs) laser pulses with $I\lambda_0^2 = 10^{17}$ W cm^{-2} μm^2 and above[1] has opened new possibilities for investigating relativistic laser–plasma interaction and corresponding generation of high harmonics. Here, I is the focussed intensity and λ_0 is the laser wavelength. Focussing the laser beam into a gas target at lower intensities ($I\lambda_0^2 = 10^{13} - 10^{15}$ W cm^{-2} μm^2), high harmonics of the laser frequency have been observed, reaching the soft x-ray region.[2] However, harmonic generation in gases relies on atomic non-linearities and becomes inefficient at higher intensities due to ionization. In the present work, we consider laser interaction with condensed matter, implying ionization in thin surface layers and making use of non-linear effects in the reflection of light from this surface to generate the harmonics. As it turns out, non-linearities of relativistic origin strongly enhance the production of high harmonics.

First experiments looking for harmonics from solid surfaces irradiated by ultrashort laser pulses have been performed recently. Using titanium sapphire laser systems ($\lambda_0 = 0.8$ μm) with focussed intensities of about 10^{17} W/cm^2 and pulse lengths of 100–150 fs,[3,4] harmonics up to the 15th order have been observed. Up to the 68th harmonic order has been detected with 2.5 ps pulses from a Nd:glass laser system ($\lambda = 1.05$ μm), reaching an intensity of 10^{19} W/cm^2 in the relativistic regime.[5] These latter results resemble those obtained earlier with nanosecond CO$_2$ laser pulses ($\lambda = 10.6$ μm)[6–9] in that the harmonics are emitted into a broad angular interval and are quite insensitive to p- or s-polarization of the incident pulse.

For theoretical interpretation, the density scale length L of the surface plasma and uniformity of the critical surface are of key importance. Layers of ablating plasma with $L \gg \lambda_0$ are formed by nanosecond pulses, whereas $L \ll \lambda_0$ is characteristic for femtosecond pulses with quite different interaction physics. However, prepulses may form an ablation layer before the short main-pulse arrives and have to be con-

trolled in experiments. Even for prepulse-free high-intensity pulses, the ponderomotive pressure acting on the overdense plasma surface may lead to non-planar distortions of the surface; Rayleigh–Taylor-like structures have been seen in two-dimensional (2D) simulations.[10,11] Ripples in the critical surface will affect angular dependence and sensitivity to polarization of the emitted harmonics.

The present work considers plane, preionized, steeply bounded plasma layers in a one-dimensional (1D) description. Oblique incidence of laser light is accommodated by following Bourdier,[12] transforming to a moving frame in which the light is normally incident. The method is described in Section II. This 1D treatment restricts the emission of reflected light (including harmonics) to the specular direction, and all effects that may lead to emission into a broader angular space in actual experiments are not accounted for. The plasma is treated kinetically by means of 1D3V (one spatial, three velocity dimensions) particle-in-cell (PIC) simulations, solving the relativistic equations of motion for a set of electrons and ions and allowing for arbitrary polarization. Densities, currents, and the electromagnetic field are defined on a 1D grid and are updated after each particle push. Details are given in Section III.

Calculations of relativistic laser plasma interaction at overdense plasma boundaries have been performed before by a number of groups.[10,13–18] For normal laser incidence, odd harmonics have been obtained in 1D and 2D PIC simulations,[13] also showing weaker even harmonics when taking into account two-dimensional effects. Investigating harmonic generation for oblique incidence in the Lorentz-boosted frame, 1D PIC simulations have been carried out by Bulanov *et al.*[17] and recently by Gibbon,[18] treating pulses with intensities up to $I\lambda_0^2 = 10^{19}$ W cm^{-2} μm^2 for oblique incidence with high numerical accuracy resolving harmonics above the noise level up to the order of 60. The 1D calculations have the advantage that one can afford a large number of time steps per laser cycle and many particles per cell such
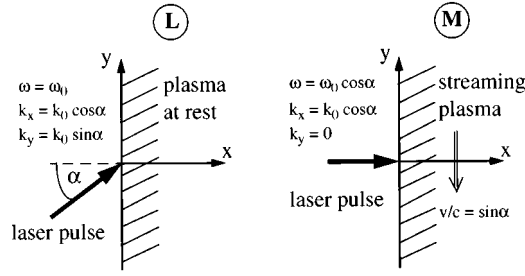
FIG. 1. Laboratory frame L with oblique laser incidence on plasma at rest and moving frame M with normal laser incidence on plasma streaming parallel to the planar surface. Light frequency ω and **k**-vector are given for both frames.

that high orders of harmonics can be resolved.

The PIC simulations presented in this paper extend those of Gibbon by investigating a larger parameter space, varying intensity, angle of incidence, polarization and plasma density. Results are presented in Section IV in the form of electron density plots and harmonic spectra. The simulations also contain information on absorption, generation of high energy electrons, wave breaking etc., but these details are found to be not so important in the present context of harmonic generation and are therefore not described here. Strong oscillations of the critical surface, however, seen in the density plots, are of central importance. They are driven by the ponderomotive force as well as by direct action of the laser field. Based on these results, a new interpretation is given for the reflected spectrum in terms of a model that is developed in Sections V–VII. The basic idea was first expressed by Bulanov et al.,[17] suggesting that it is the reflection from an oscillating mirror (the critical surface) which generates the harmonics.

This model is worked out here in detail and is shown to reproduce the spectra obtained from the PIC simulations almost quantitatively. Typically, one oscillation amplitude is adjusted, as well as additional ones in cases of more complex surface motion. In Section V, a closed set of fully relativistic equations for the electromagnetic field in the plasma is derived, describing the plasma as a cold relativistic fluid. These equations had been given before by Sprangle et al.[19] for normal incidence and are generalized here to the case of oblique incidence. General selection rules are deduced from these equations for the polarization of odd and even harmonics in Section VI. Section VII is then devoted to the surface model, treating both the retarded reflection from the moving surface and the relativistic dynamics of the surface.

II. BASIC EQUATIONS FOR OBLIQUE INCIDENCE

The present investigation is restricted to one-dimensional geometry and considers a plane plasma layer with a sharp surface. The configuration is sketched in Fig. 1. To incorporate the oblique incidence of laser light, we use Bourdier's method[12,15,17] and make a Lorentz transformation from the laboratory frame L to a frame M, moving in y-direction parallel to the surface such that the pulse is nor-

mally incident in frame M. For an angle of incidence α, this is achieved with a frame velocity $\mathbf{v}_f = c \sin \alpha \hat{\mathbf{y}}$ which corresponds to

$$\beta = v_f/c = \sin \alpha, \qquad \Gamma = 1/\sqrt{1-\beta^2} = 1/\cos \alpha. \qquad (1)$$

While the plasma is at rest in L, it streams in M with $-\mathbf{v}_f$. In changing from L to M, the frequency ω_0 of the wave and the k-vector with absolute value $k_0 = \omega_0/c$ transform according to

$$\begin{aligned}
\omega^L &= \omega_0, & \mathbf{k}^L &= (k_0 \cos \alpha, \, k_0 \sin \alpha, \, 0), \\
\omega^M &= \omega_0 \cos \alpha, & \mathbf{k}^M &= (k_0 \cos \alpha, \, 0, \, 0),
\end{aligned} \qquad (2)$$

such that the relation $\omega^M = ck^M$ is preserved. The field amplitudes of the incident electromagnetic wave in L and M are for p-polarization

$$\begin{aligned}
\mathbf{E}^L &= E_0(-\hat{\mathbf{x}} \sin \alpha + \hat{\mathbf{y}} \cos \alpha), & c\mathbf{B}^L &= E_0\hat{\mathbf{z}}, \\
\mathbf{E}^M &= E_0\hat{\mathbf{y}} \cos \alpha, & c\mathbf{B}^M &= E_0\hat{\mathbf{z}} \cos \alpha,
\end{aligned} \qquad (3)$$

and for s-polarization

$$\begin{aligned}
\mathbf{E}^L &= E_0\hat{\mathbf{z}}, & c\mathbf{B}^L &= E_0(\hat{\mathbf{x}} \sin \alpha - \hat{\mathbf{y}} \cos \alpha), \\
\mathbf{E}^M &= E_0\hat{\mathbf{z}} \cos \alpha, & c\mathbf{B}^M &= -E_0\hat{\mathbf{y}} \cos \alpha.
\end{aligned} \qquad (4)$$

Apparently, the field amplitudes are reduced by a factor $\cos \alpha$, but we notice that the dimensionless amplitude $a_0 = eE_0/m\omega_0c$ remains invariant. The unperturbed plasma density in M, $n_{0M} = n_{0L}/\cos \alpha$, is increased by the Γ-factor compared to the unperturbed density n_{0L} in L.

The basic equations given below refer to the M-frame; for convenience, the label M is dropped. They depend only on one spatial coordinate, the x-axis. The assumption of translational symmetry in M implies that possible plasma perturbations in y- or z-direction are excluded and that the description is restricted to light reflection in specular direction. Maxwell's equations then read

$$\left(\partial_x^2 - \frac{1}{c^2}\partial_t^2\right)\mathbf{A}(x,t) = -\frac{1}{\varepsilon_0 c^2}\mathbf{j}_\perp(x,t), \qquad (5a)$$

$$\partial_x^2\Phi(x,t) = -\frac{1}{\varepsilon_0}\varrho(x,t), \qquad (5b)$$

$$\mathbf{E} = \mathbf{E}_l + \mathbf{E}_\perp, \qquad \mathbf{E}_l = -\hat{\mathbf{x}}\partial_x\Phi(x,t),$$

$$\mathbf{E}_\perp = -\partial_t\mathbf{A}(x,t), \qquad (5c)$$

$$\mathbf{B}(x,t) = \nabla \times \mathbf{A}(x,t). \qquad (5d)$$

Here, we use the Coulomb gauge ($\nabla \cdot \mathbf{A} = 0$) in frame M. All final results will be given in **E** and **B** fields transformed back into frame L and are independent of the gauge. The equations of motion for plasma particles of mass m and charge q are

$$d_t(m\gamma\mathbf{v}) = q(\mathbf{E} + \mathbf{v} \times \mathbf{B}), \qquad \gamma = \frac{1}{\sqrt{1-(v/c)^2}}. \qquad (6)$$

Lichters, Meyer-ter-Vehn, and Pukhov

This set of equations is treated in two ways, first, numerically by means of kinetic simulations using a particle-in-cell (PIC) code, and second, analytically in terms of a cold relativistic fluid model.

III. PIC CODE

For the kinetic simulations, a 1D3V relativistic electromagnetic particle-in-cell (PIC) code has been developed. The plasma is represented by macro-particles that have three velocity components and contribute to charge and current densities on a one-dimensional spatial grid. This allows for arbitrary polarization of the incident pulse. In each time step, the particles move according to the relativistic equation of motion (6). The electromagnetic fields $\mathbf{E}$ and $\mathbf{B}$ are calculated from Maxwell's equations. The longitudinal electric field is obtained from the charge density, solving Poisson's equation, and the transverse electromagnetic fields from the transverse current density, solving the wave equation. The laser pulse is introduced as a time-dependent boundary condition for the transverse fields at the front side of the simulation box.

The basic algorithm for solving Maxwell's equations is that of Birdsall and Langdon.[20] It includes a properly time-centered ''leap frog'' scheme for pushing the particles. The method of Fourier transform is used to solve Poisson's equation, and the transverse fields are integrated along vacuum characteristics. The spatial resolution of the skin layer sets the most stringent numerical condition. Typically we use 1000 cells per wavelength (cell size Δx), implying 1000 timesteps Δt per laser cycle to satisfy $\Delta x = c \Delta t$. This leads to 80 cells for the skin depth of a four times overcritical plasma and gives acceptable accuracy.

The simulation box has a length of $\approx 8\lambda_0$, and the plasma occupies a region of thickness $1\lambda_0$ in the middle of the box, initially. This leaves enough vacuum space to the left and the right of the plasma to prevent particles from reaching the boundaries. We use 100 particles per cell, implying more than 10^5 particles in total. An initial electron temperature of 50 eV is chosen for numerical reasons. One time step takes 4 seconds of CPU time on an IBM RISC/6000 model 250 workstation. A typical run using a laser pulse of 20 periods duration needs 24 hours of CPU time and 10 Mbytes of memory. The code can deal with arbitrary initial density profiles and with both electron and ion dynamics. In the present work, however, we restrict ourselves to uniform layers with a sharp surface boundary. Also, the ions are kept fixed, since they move very little on the time scale of the short pulses and are found to have little effect on the generation of harmonics.

The spectra shown in this paper are power spectra of the electric field $\mathbf{E}$, taken in frame L. They contain the field of the incident as well as the reflected light. The field $\mathbf{E}(x_0,t)$ as a function of time is taken at a position x_0 in the vacuum region in front of the irradiated surface. Its discrete Fourier transform, averaged over the pulse duration T, is given by

$$\mathbf{E}(\omega_j) = \frac{1}{T} \sum_{k=0}^{N-1} \Delta t\, \mathbf{E}(t_k) \exp(i\omega_j t_k),$$

where $\omega_j = j\Delta\omega$ $(j = -N/2, \ldots, N/2)$, $\Delta\omega = 2\pi/T$, $t_k = k\Delta t$ $(k = 0, \ldots, N-1)$, $\Delta t = T/N$. The power spectrum $2|\mathbf{E}(\omega_j)|^2$ is related to the average power of the signal $\mathbf{E}(x_0,t)$ by Parseval's theorem,

$$\frac{1}{T} \sum_{k=0}^{N-1} \Delta t\, \mathbf{E}^2(t_k) = |\mathbf{E}(\omega=0)|^2 + \sum_{j=1}^{N/2} 2|\mathbf{E}(\omega_j)|^2.$$

We plot the power spectrum $2|\mathbf{E}(\omega_j)/E_r|^2$, normalized to relativistic units $E_r = m\omega_0 c/e$. Except for the fundamental peak, the plotted spectrum represents the normalized spectral intensity of the reflected light. The fundamental peak contains also some fraction of the incident laser light.

IV. RESULTS OF PIC SIMULATIONS

A central concern of this paper is to investigate the relation between plasma surface oscillations and harmonic generation. This will become explicit by means of the model developed in the subsequent sections. The PIC simulations, obtained with the 1D code just described and presented in this section, serve as numerical experiments to guide intuition and to test model assumptions. Harmonics spectra are given together with contour plots of electron density to demonstrate the laser excitation of the plasma surface. We discuss a couple of cases, varying

(1) field strength $a_0 = eE_0/m\omega_0 c = (I\lambda_0^2/1.37 \times 10^{18}\text{ W cm}^{-2}\ \mu\text{m}^2)^{1/2}$,
(2) initial electron density n_0/n_c in units of the critical density $n_c = \varepsilon_0 m\omega_0^2/e^2$,
(3) angle of incidence α, and
(4) polarization.

The envelope of the incident field is varied according to

$$P(t) = \begin{cases} \sin^2(\pi t/T) & \text{for } 0 \leqslant t \leqslant T, \\ 0 & \text{else,} \end{cases}$$

within the pulse duration $T = 20\tau$, where $\tau = 2\pi/\omega_0$ is the time of one laser cycle.

We start with a simple case. A laser beam with $I\lambda_0^2 = 3.4 \times 10^{17}$ W cm^{-2} μm^2, corresponding to $a_0 = 0.5$, is normally incident on the plasma layer shown in Fig. 2. Electron density is plotted, using a grey scale. The black part to the right represents the shelf density $n_0/n_c = 7$. The ion density is not shown; it is fixed with a sharp surface at $x = 0$. One sees that the electron density oscillates about this surface. The density decreases in the oscillating zone, as indicated by the contour lines for the critical surface $n/n_c = 1$ and for $n/n_c = 0.1$. One may notice that the different contour lines oscillate with different phases.

The spectrum of the reflected light is shown in Fig. 3. One observes a few harmonics which quickly drop in amplitude; a characteristic feature is that only odd harmonics at frequencies $3\omega_0$, $5\omega_0$, $7\omega_0$, ... show up. They can be understood as reflection from the oscillating mirror represented by the critical surface. The corresponding model spectrum is given by the diamonds in Fig. 3. The surface amplitude, adjusted to $0.011\lambda_0$, is close to the amplitude of the critical surface obtained in the PIC simulations and shown in Fig. 2.
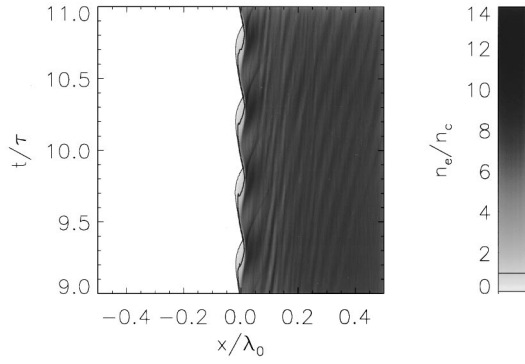
FIG. 2. Electron density $n(x,t)$ given by a grey scale in units of the critical density n_c versus coordinate x and time t in units of laser wavelength λ_0 and cycle time τ. A laser pulse with linear polarization and maximum intensity $I\lambda_0^2 = 3.4 \times 10^{17}$ W cm$^{-2}\mu$m^2 ($a_0 = 0.5$) is normally incident on the uniform layer with density $n_0/n_c = 7$. The intensity varies $\propto \sin^4(\pi t/T)$ with pulse duration $T = 20\tau$. The time window shown corresponds to two cycles around the pulse maximum. The initial surface position is $x/\lambda_0 = 0$. The contour lines mark the critical density $n = n_c$ and $n = 0.1 n_c$, respectively.

FIG. 3. Harmonic spectrum for the case of Fig. 2 with parameters: $a_0 = 0.5$, $n_0/n_c = 7$, $\alpha = 0$, linear polarization. Scaled intensity is plotted versus scaled frequency; for details see Section III. The diamonds refer to the oscillating mirror model with $X(t) = -0.011\lambda_0 \cos(2\omega_0 t)$; see Section VII.

In the present case, the incident pulse is linearly polarized such that the ponderomotive force $\propto (1 - \cos(2\omega_0 t))$ has an oscillating component, driving the surface at twice the laser frequency. We carried out the same calculation also for circular polarization. In this case, the ponderomotive force is quasi-steady, and we find neither surface oscillations nor any harmonics.

Let us now change the density to $n_0/n_c = 4$, leaving all other parameters as before. Lower density implies smaller restoring forces and therefore larger amplitudes of the electron surface oscillations. In addition, the plasma frequency $\omega_p = 2\omega_0$ for $n_0/n_c = 4$ is in resonance with the driving force, further enhancing the oscillations. They are plotted in Fig. 4. The critical surface oscillates with an amplitude of about $0.05\lambda_0$, whereas the $n/n_c = 0.1$ surface is almost stationary. Density waves are also seen in the bulk plasma; however, they have almost no effect on the harmonic spectrum and are not further considered in this paper. The spectrum corresponding to this case is shown in Fig. 5. Again, odd harmonics are obtained and are well reproduced by the model. Due to the larger oscillations, they now extend to higher orders.
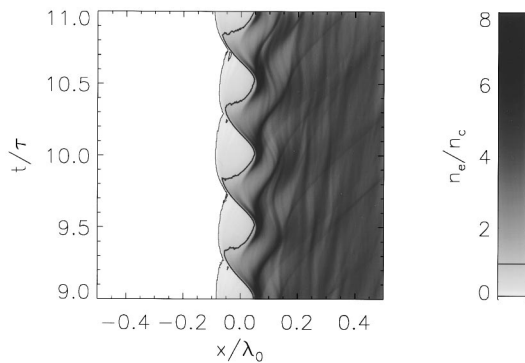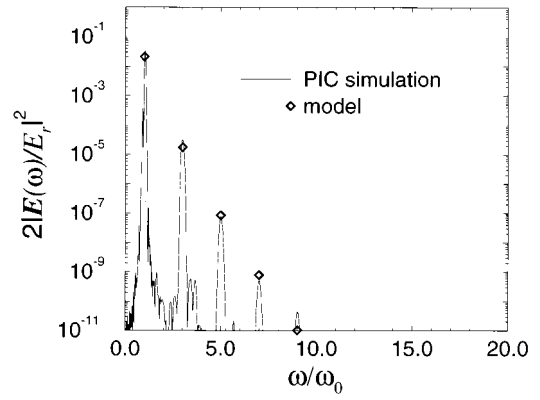
Figures 6 and 7 demonstrate the effect of increasing the intensity to $I\lambda_0^2 = 1.4 \times 10^{18}$ W cm$^{-2}\mu$m^2; it corresponds to the relativistic threshold of $a_0 = 1$. The critical surface now accelerates to velocities of about $0.6c$, and non-linear effects modify its trajectory, giving it a tooth-like shape. As expected, the emission of harmonics goes up significantly. For example, the intensity of the 15th harmonic, I_{15}/I_0, increases by a factor of 500 when going from $a_0 = 0.5$ to $a_0 = 1$; here, $I_0 = (3/16)a_0^2$ is the average intensity of the incident pulse. The model describes these trends remarkably well. However, the slight redshift ($\Delta\omega/\omega \lesssim 0.01$) observed in Fig. 7 with respect to exact multiples of ω_0 is not yet understood. Another peculiar feature are the smaller peaks in between the odd harmonics. They show up only in the resonant case, $\omega_p = 2\omega_0$, and disappear when detuning the plasma frequency, e.g. by setting $n_0/n_c = 5$. Also their origin needs further investigation.

Next, we consider oblique incidence ($\alpha = 30°$) of s-polarized light for $a_0 = 0.5$ and $n_0/n_c = 4$. The surface oscillations in Fig. 8 have smaller amplitude than those obtained for normal incidence, since for oblique incidence the driving power per area is reduced. Correspondingly, the spectrum given in Fig. 9 falls off more rapidly. A more drastic change concerns p-polarized even harmonics which now
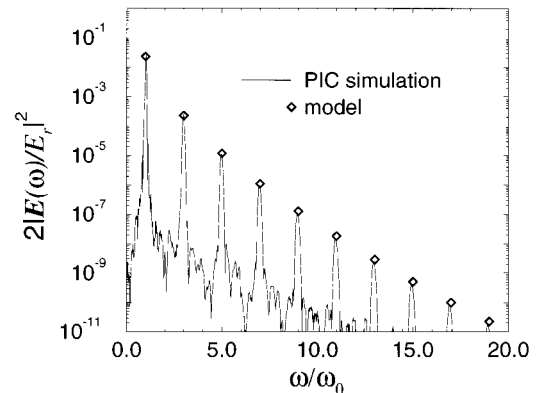

FIG. 4. Electron density for parameters: $a_0 = 0.5$, $n_0/n_c = 4$, $\alpha = 0$, linear polarization.

FIG. 5. Spectrum corresponding to the case of Fig. 4; the diamonds refer to the model with $X(t) = -0.033\lambda_0 \cos(2\omega_0 t - \pi/2)$.

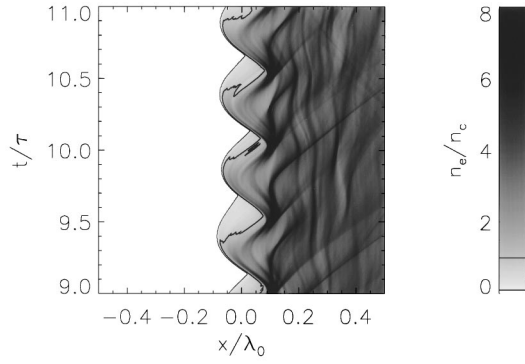Lichters, Meyer-ter-Vehn, and Pukhov

FIG. 6. Electron density for parameters: $a_0 = 1$, $n_0/n_c = 4$, $\alpha = 0$, linear polarization.

FIG. 7. Spectrum corresponding to the case of Fig. 6; the diamonds refer to the model with $X(t) = -0.052\lambda_0 \cos(2\omega_0 t - \pi/2)$.

appear in addition to the odd *s*-polarized harmonics. The underlying selection rules will be derived in Section VI. Again, the general roll-off of the spectrum is well described by the standard model (diamonds), but it strongly overestimates the intensity of the even harmonics. Possible reasons for this failure are discussed in Section VIIC, including a model modification leading to the crosses in Fig. 9.

Finally, oblique incidence ($\alpha = 30°$) of *p*-polarized light is also considered for $a_0 = 0.5$ and $n_0/n_c = 4$. The electron surface is then driven by the normal component of the **E** field of the laser light, oscillating at frequency ω_0, in addition to the ponderomotive force, oscillating at $2\omega_0$. This leads to more complex motion of the surface and to reflected spectra containing both odd and even harmonics, as we see in Figs. 10 and 11. The dramatic new feature in the density plot are the flares of low density plasma, marked by the $n/n_c = 0.1$ density contour. This plasma is extracted from the surface once in each laser cycle and then reinjected into the bulk plasma. This mechanism of so-called *vacuum heating* has been described in detail by Brunel.[21]

The corresponding spectrum in Fig. 11 consists of odd and even harmonics, all *p*-polarized as the incident light; *s*-polarized light is emitted only at the noise level (see the dashed line). It is interesting to note that again the PIC spectrum can be well reproduced (with the exception of the second harmonic) by the model spectrum, this time adjusting two amplitudes which is the very minimum to account for the ω_0 and the $2\omega_0$ surface mode and is certainly insufficient
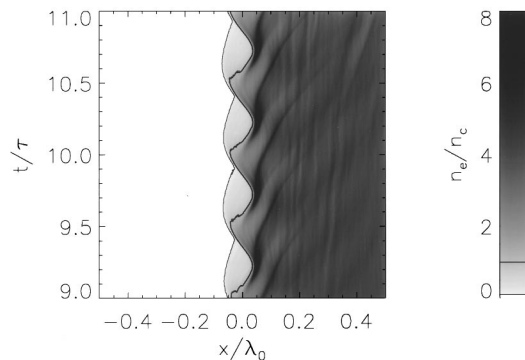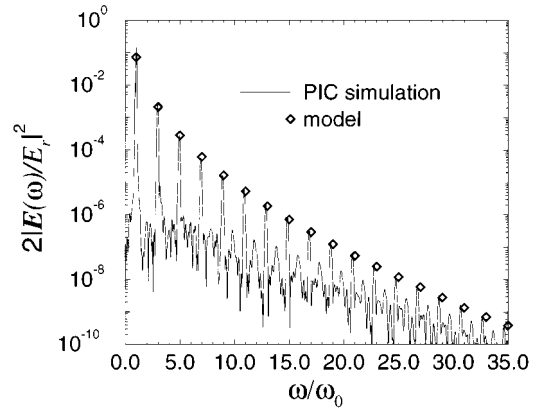
to describe the violent surface excitation seen in Fig. 10. It indicates that the kinetics of vacuum heating involving underdense plasma has little influence on the harmonic spectrum which in turn is determined by the motion of the denser plasma region close to the critical surface. We also notice that the strength of the odd harmonics is almost identical to those obtained in Fig. 5 for normal incidence and otherwise same parameters. The decrease of ponderomotive drive is compensated in this case by the action of the normal component of the electric field. For $a_0 = 0.5$ and $n_0/n_c = 4$, harmonics are strongest at about 30°. Further results for oblique incidence of more intense ($a_0 = 3$) pulses will be given in Section VIIC.

V. COLD RELATIVISTIC PLASMA FLUID EQUATIONS

In this section, a set of fluid equations, valid in the moving frame M, is derived. It will help to interpret the fully self-consistent kinetic simulations based on the PIC code. The plasma is assumed to be a cold electron fluid with a static background of ions, having the uniform velocity $-c\hat{\mathbf{y}} \sin \alpha$. Switching from the particle description to a Euler fluid description, velocity **v** and momentum **p**, related by

FIG. 8. Electron density for oblique incidence of *s*-polarized light with parameters: $a_0 = 0.5$, $n_0/n_c = 4$, $\alpha = 30°$.
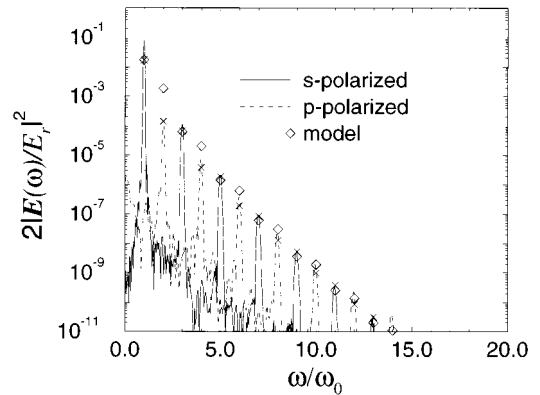

FIG. 9. Spectrum corresponding to the case of Fig. 8; the diamonds refer to the model with $X(t) = -0.023\lambda_0 \cos(2(\omega_0 \cos\alpha)t - \pi/2)$ and the crosses to the modified model explained in Section VIIC.
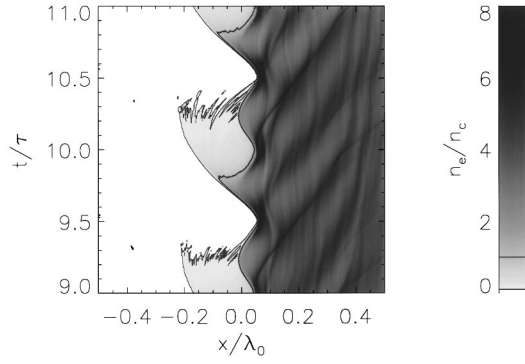
FIG. 10. Electron density for oblique incidence of p-polarized light with parameters: $a_0 = 0.5$, $n_0/n_c = 4$, $\alpha = 30°$.

FIG. 11. Spectrum corresponding to the case of Fig. 10; diamonds refer to $X(t) = +0.027\lambda_0 \sin((\omega_0 \cos \alpha)t) - 0.023\lambda_0 \cos(2(\omega_0 \cos \alpha)t - \pi/2)$ and $\alpha = 30°$.

$$\mathbf{p} = m\gamma\mathbf{v}, \qquad \gamma = \sqrt{1 + \left(\frac{\mathbf{p}}{mc}\right)^2}, \tag{7}$$

are now interpreted as fluid functions $\mathbf{v}(x,t)$ and $\mathbf{p}(x,t)$, depending on space and time. At zero temperature, this is admitted since the velocity distribution is sharply peaked and all fluid particles at position x and time t have the same velocity $\mathbf{v}(x,t)$. In this fluid picture, the total time derivatives d_t have to be interpreted as $d_t = \partial_t + v_x\partial_x$.

Starting from Maxwell's equations (5) and the equation of motion (6), we first derive the kinetic energy balance

$$d_t\gamma = \frac{q}{mc^2}(-v_x\partial_x\Phi - \mathbf{v}_\perp \cdot \partial_t\mathbf{A}) \tag{8}$$

and the continuity equation

$$\partial_t\varrho + \nabla\mathbf{j} = \partial_t\varrho + \partial_x j_l = 0. \tag{9}$$

Next, the longitudinal momentum p_l is written in the form

$$d_t p_l = q(-\partial_x\Phi + \mathbf{v}_\perp \cdot \partial_x\mathbf{A}), \tag{10a}$$

and for the transverse momentum $\mathbf{p}_\perp$ one has

$$d_t(\mathbf{p}_\perp + q\mathbf{A}) = 0, \tag{10b}$$

because of translational invariance in y- and z-direction. The conservation of the generalized transverse momentum (10b) leads to

$$\mathbf{p}_\perp = m\gamma\mathbf{v}_\perp = \mathbf{p}_\perp^0 - q\mathbf{A}, \tag{11}$$

where $\mathbf{p}_\perp^0 = m\gamma^0\mathbf{v}_\perp^0 = -\hat{\mathbf{y}}mc \tan \alpha$ denotes the initial transverse momentum, corresponding to plasma streaming in negative y-direction. For $t<0$, the vector potential is equal to zero inside the plasma ($x>0$); the initial distribution of electrons and ions is given by $n_e(x) = Zn_i(x) = n_{0M}\Theta(x)$, where n_{0M} is the electron particle density of the unperturbed plasma in frame M.

Equation (11) is used to eliminate the transverse velocities $\mathbf{v}_\perp$ in Equations (5a), (8) and (10a). Notice that the transverse current in Equation (5a) contains electron and ion contributions, $\mathbf{j}_\perp = -e(n_e\mathbf{v}_{\perp,e} - Zn_i\mathbf{v}_{\perp,i})$. After these substitutions, Equations (8) and (10a) are combined in an equation of motion for the longitudinal velocity v_x. The final result is expressed in terms of the scaled dimensionless quantities
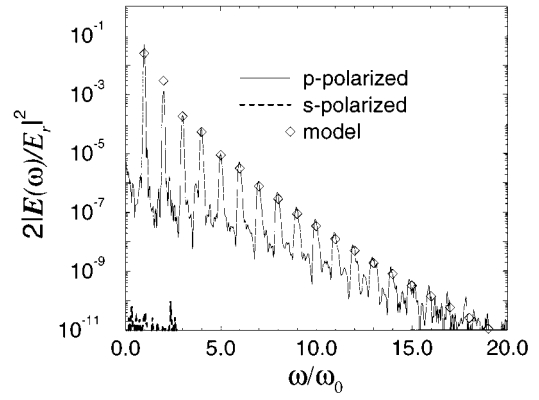
$$\mathbf{a} = \frac{e\mathbf{A}}{mc}, \qquad \varphi = \frac{e\Phi}{mc^2}, \qquad n = \frac{n_e}{n_{0M}}, \qquad \beta_x = \frac{v_x}{c}, \tag{12}$$

which satisfy the equations

$$\left(\partial_x^2 - \frac{1}{c^2}\partial_t^2\right)\mathbf{a} = \left(\frac{\omega_p}{c}\right)^2\left[\frac{n}{\gamma \cos \alpha}(\mathbf{a} - \hat{\mathbf{y}} \tan \alpha)\right.$$

$$\left. + \hat{\mathbf{y}}\tan\alpha\, \Theta(x)\right], \tag{13a}$$

$$\gamma = \sqrt{\frac{1 + (\mathbf{a} - \hat{\mathbf{y}} \tan \alpha)^2}{1 - \beta_x^2}}, \tag{13b}$$

$$\partial_x^2\varphi = \left(\frac{\omega_p}{c}\right)^2\frac{1}{\cos \alpha}(n - \Theta(x)), \tag{13c}$$

$$\partial_t n + c\partial_x(n\beta_x) = 0, \tag{13d}$$

$$d_t\beta_x = \frac{c}{\gamma}(1 - \beta_x^2)\partial_x\varphi - \frac{1}{\gamma^2}(c\partial_x + \beta_x\partial_t)$$

$$\times\left(\frac{\mathbf{a}^2}{2} - \mathbf{a}\cdot\hat{\mathbf{y}} \tan \alpha\right). \tag{13e}$$

The quantities $\mathbf{a}$, φ, n, β_x depend on coordinate x and time t. The plasma frequency, $\omega_p^2 = n_0 e^2/m\varepsilon_0$, is determined from the unperturbed electron density n_0 in frame L and the rest mass m of the electron. Equations (13) are written such that the dependence on the angle of incidence α appears explicitly; for normal incidence ($\alpha = 0$), they have been given before by Sprangle et al.[19]

On the right-hand side of the longitudinal equation of motion (13e), three force terms occur. The first term corresponds to the longitudinal electric force $\propto \partial_x\varphi$, arising from charge separation. The second term contains the ponderomotive force $\propto \mathbf{a}^2$. The third term $\propto \mathbf{a}\cdot\hat{\mathbf{y}}$ corresponds to the $\mathbf{E}$ component of the light field in frame L that acts perpendicular to the plasma surface in the case of oblique incidence of p-polarized light. In the M frame, this term appears in first order as a Lorentz force in x-direction, arising from the magnetic field $B_z \propto \partial_x a_y$ and the constant frame velocity. One may notice that the plasma dynamics as described by Equa-

Lichters, Meyer-ter-Vehn, and Pukhov

TABLE I. Selection rules for polarization of harmonics (s-polarized, p-polarized) depending on polarization of the incident pulse for oblique and normal incidence.

Incident pulse	Odd harmonics	Even harmonics
Oblique incidence		
s	s	p
p	p	p
Circular	s,p	s,p
Normal incidence		
Linear	Linear	···
Circular	···	···

tions (13b)–(13e) are driven only by the square of the field $\mathbf{a}^2$, in cases when $\mathbf{a}\cdot\hat{\mathbf{y}}=0$, i.e., for oblique incidence of s-polarized light or normal incidence and arbitrary polarization. In these cases, $n(x,t)$, $\beta_x(x,t)$, and $\varphi(x,t)$ contain only even Fourier components of ω_0; this general conclusion is important in the following discussion.

VI. SELECTION RULES

Selection rules with respect to parity (i.e. odd, even) and polarization of emitted harmonics are apparent from the PIC results discussed in Section III. They are summarized in Table I. In the present section, we deduce them from Equations (13a)–(13e). Concerning the light field $\mathbf{a}$, let us look at component a_y for the p-polarized and component a_z for the s-polarized harmonics, separately. Equation (13a) gives

$$\left(\partial_x^2-\frac{1}{c^2}\partial_t^2\right)a_y=\left(\frac{\omega_p}{c}\right)^2 s_y(x,t),$$
$$\left(\partial_x^2-\frac{1}{c^2}\partial_t^2\right)a_z=\left(\frac{\omega_p}{c}\right)^2 s_z(x,t),$$
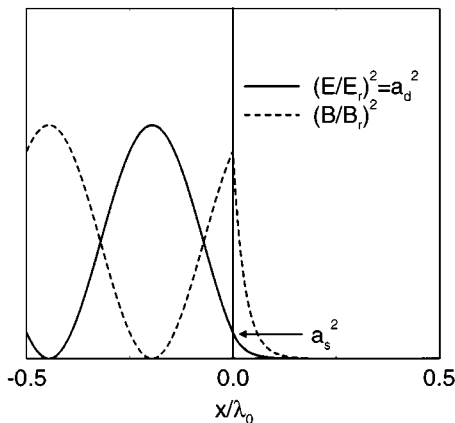(14)

with the source terms

FIG. 12. Scaled electric and magnetic field of the standing wave at the plasma surface according to Equation (16). A skin depth $\lambda_0/6\pi$ is assumed, corresponding to $n_0/n_c=9$ and $\alpha=0$.

$$s_y(x,t)=n\sqrt{1-\beta_x^2}\frac{a_y-\tan\alpha}{\sqrt{1+(\mathbf{a}\cos\alpha)^2-a_y\sin2\alpha}}+\tan\alpha\Theta(x),$$
$$s_z(x,t)=n\sqrt{1-\beta_x^2}\frac{a_z}{\sqrt{1+(\mathbf{a}\cos\alpha)^2-a_y\sin2\alpha}}.$$
(15)

In the following, it is important to recall that we are considering the surface of overdense plasma at which a major part of the incident light is reflected. Inside the plasma, the vector potential decays rapidly. The skin layer of thickness d_s is much smaller than λ_0. The source terms $s_y(x,t)$ and $s_z(x,t)$, which generate the harmonics, are therefore sharply localized at the surface, and we need the driving field $\mathbf{a}_d(x,t)$ close to $x\approx0$. Its leading component oscillates with the fundamental frequency ω_0 and can be obtained from the linearized version of Equations (13a)–(13e) in the approximate form

$$\mathbf{a}_d(x,t)\simeq\begin{cases}-2\mathbf{a}_0\sin(kx-\theta)\sin(\omega t); & x<0,\\ \mathbf{a}_s\exp(-x/d_s)\sin(\omega t); & x\geq0,\end{cases}$$
(16)

where $d_s=(c/\omega_p)/\sqrt{1-(\omega_0/\omega_p)^2}$, $k=k_0\cos\alpha$ and $\omega=\omega_0\cos\alpha$. In the following, we discuss the pure s-polarized and the pure p-polarized case for which the global phase in Equation (16) can be chosen such that $\mathbf{a}_d=0$ for $t=0$. This solution is plotted in Fig. 12 for $\alpha=0$. For $x<0$, it represents a standing wave, formed by the superposition of the incident laser wave with amplitude $\mathbf{a}_0$ and the reflected wave. The evanescent field for $x\geq0$ has the amplitude $\mathbf{a}_s$ at the surface. Carefully investigating matching conditions at $x=0$, one obtains for s-polarization ($\mathbf{a}=a\hat{\mathbf{z}}$)

$$\mathbf{a}_s=2\frac{\omega_0\cos\alpha}{\omega_p}\mathbf{a}_0,$$
$$\tan\theta=\frac{\omega_0\cos\alpha}{\omega_p}\frac{1}{\sqrt{1-(\omega_0\cos\alpha/\omega_p)^2}},$$
(17)

and for p-polarization ($\mathbf{a}=a\hat{\mathbf{y}}$)

$$\mathbf{a}_s=2\frac{\omega_0}{\omega_p}\sqrt{\frac{1-(\omega_0\cos\alpha/\omega_p)^2}{\cos^2\alpha-(\omega_0/\omega_p)^2\cos2\alpha}}\mathbf{a}_0,$$
$$\tan\theta=\frac{\omega_0}{\omega_p}\frac{\sqrt{1-(\omega_0\cos\alpha/\omega_p)^2}}{\cos\alpha(1-(\omega_0/\omega_p)^2)}.$$
(18)

In the next section, we use this form of the driving field to model harmonics explicitly. Here, all we need to deduce the selection rules is the observation that it is essentially the fundamental component $\mathbf{a}_d(x,t)\propto\sin((\omega_0\cos\alpha)t)$ in $\mathbf{a}$ which generates the harmonics when inserted into the source terms (15).

Apparently, there are three non-linear factors in Equation (15) that lead to harmonics:

(1) the density n, including the critical surface and its motion,
(2) the term $\sqrt{1-\beta_x^2}$ containing the longitudinal velocity, and

(3) the term $(\mathbf{a} - \hat{\mathbf{y}} \tan\alpha)/\sqrt{1+(\mathbf{a}\cos\alpha)^2-a_y\sin2\alpha}$ containing the vector potential $\mathbf{a}$ and the angle of incidence.

Concerning the polarizations a_y and a_z, they are coupled in Equations (14) in two ways. First, they are coupled through the electron density $n(x,t)$ and the longitudinal velocity $\beta_x(x,t)$ which are both driven by $\mathbf{a}$; surface motion, i.e. the oscillation of $n(x,t)$ around the fixed ion surface, leads to a coupling even when the other factors were kept constant. Second, there is a relativistic coupling due to the appearance of both a_y and a_z in the square root denominator. These square roots originate from the relativistic γ-factor (13b). Let us first consider the case of normal incidence.

A. Normal incidence

For $\alpha=0$, there is no difference between s- and p-polarization, and the source terms (15) become identical. Let us assume incident light linearly polarized in the z-direction. The relevant source term then reads

$$s_z(x,t)=n(x,t)\sqrt{1-\beta_x^2(x,t)}\frac{a_z(x,t)}{\sqrt{1+a_z^2(x,t)}}, \qquad (18')$$

where $a_z(x,t)$ is approximately of form (16) and its spectrum is dominated by the fundamental. Recall that $n(x,t)$ and $\beta_x(x,t)$ are even functions of a_z in this case. Correspondingly, the source term $s_z(x,t)$ is an odd function of the driving field, and therefore normal incidence of linearly polarized light generates only odd harmonics of the same polarization as the incident light.

For circular polarization, the vector potential of the normally incident light rotates with an amplitude $|\mathbf{a}(x,t)|$ which is independent of time. Therefore the ponderomotive force acting on the plasma surface is constant, and *no* harmonics are generated at all.

B. Oblique incidence of *s*-polarized light

In this case, the driving field $\mathbf{a}_d(x,t)=a_z(x,t)\hat{\mathbf{z}}$ is incident in the (x,y) plane under an angle $\alpha>0$ with respect to the normal, and the two source terms are

$$s_y(x,t)=n(x,t)\sqrt{1-\beta_x^2(x,t)}\frac{-\tan\alpha}{\sqrt{1+[a_z(x,t)\cos\alpha]^2}}$$
$$+\tan\alpha\,\Theta(x), \qquad (19a)$$

$$s_z(x,t)=n(x,t)\sqrt{1-\beta_x^2(x,t)}\frac{a_z(x,t)}{\sqrt{1+[a_z(x,t)\cos\alpha]^2}}. \qquad (19b)$$

Again, $n(x,t)$ and $\beta_x(x,t)$ are even functions of $a_z(x,t)$, and $s_z(x,t)$ produces only s-polarized odd harmonics as in the case of normal incidence. For $\alpha>0$, however, the source $s_y(x,t)$ is also non-zero and generates p-polarized even harmonics. For small α, they are weaker than the odd harmonics and disappear completely for normal incidence.

C. Oblique incidence of *p*-polarized light

Now one has $\mathbf{a}_d(x,t)=a_y(x,t)\hat{\mathbf{y}}$, and the source terms are

$$s_y(x,t)=n(x,t)\sqrt{1-\beta_x^2(x,t)}$$
$$\times\frac{a_y(x,t)-\tan\alpha}{\sqrt{1+[a_y(x,t)\cos\alpha]^2-a_y(x,t)\sin2\alpha}}$$
$$+\tan\alpha\,\Theta(x), \qquad (20a)$$

$$s_z(x,t)=0. \qquad (20b)$$

Apparently, p-polarized incident light generates only p-polarized harmonics. Since the driving term in Equation (13e) has the form $(a_y^2/2 - a_y\tan\alpha)$ in this case, the functions $n(x,t)$ and $\beta_x(x,t)$ contain both even and odd Fourier components, and therefore both odd and even harmonics are generated. The even ones vanish for $\alpha\rightarrow0$. It has been shown by von der Linde *et al.*[22] that the second harmonic is p-polarized for s- as well as p-polarized incident light. The present results generalize this observation to any even harmonic.

Though we have derived the selection rules here using the approximate expression (16) of the driving field for simplicity, one should notice that they hold in a more rigorous sense. Even when using the total vector potential $\mathbf{a}$ in Equations (15), including the full spectrum instead of just the fundamental $\mathbf{a}_d$, one arrives at the same conclusions by iterating the arguments of this section. Of course, in practice the selection rules may be violated by 2D effects, e.g. due to finite size of the focal spot, hole boring and Rayleigh–Taylor instabilities.

VII. THE OSCILLATING MIRROR MODEL

In this section, a model is developed to interpret the harmonic spectra in simple terms as reflected light from a moving mirror. An essential point is to account for retarded emission from the oscillating source. The basic idea was first proposed by Bulanov *et al.*[17] Here, we develop it in detail.

We assume that the electron distribution has a sharp surface described by the coordinate $X(t)$. It represents an effective surface from which the light is reflected and which is located close to the critical surface. The electron density is then modelled in the form

$$n(x,t)=\Theta(x-X(t)), \qquad (21)$$

where $\Theta(x)$ is the step function. The configuration is illustrated in Fig. 13. The ion density remains fixed with a sharp surface at $x=0$. In addition, the laser field that drives the density and the transverse current at the surface is set in the following to
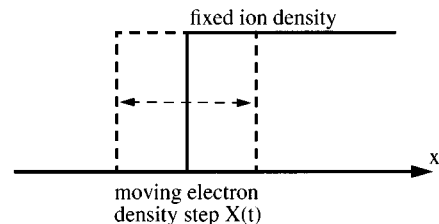

FIG. 13. Schematic plot of model electron density (dashed line) with surface at $X(t)$, oscillating relative to the fixed ion density (solid line).

$$\mathbf{a}(x,t)=\mathbf{a}_d(x-X(t),t), \tag{22}$$

where $\mathbf{a}_d(x,t)$ is given by Equation (16). This means in particular that the skin layer with thickness $\ell_s \approx c/\omega_p \ll \lambda_0$ moves as a whole with the surface. It also means that dissipative processes leading to light absorption at the surface[10,14–16] are not accounted for. One should realize that Equations (21) and (22) are introduced here as rough model assumptions, motivated by the PIC results of Section IV. The hope is to reproduce the general roll-off of the PIC spectra in this way.

In particular, we represent $X(t)$ by a few harmonic modes and adjust the amplitudes by comparing with the PIC spectra. For s-polarization and intensities $a < 1$, the surface is driven more or less harmonically by the ponderomotive force $\propto (1 - \cos(2(\omega_0 \cos \alpha)t))$, and a single term

$$X(t) \simeq -X_s \cos(2(\omega_0 \cos\alpha)t - \phi) \tag{23}$$

is taken. Here, ϕ is the relative phase between the driving field and the surface oscillation; it is expected to be $\phi \approx 0$ for cases with $\omega_p \gg 2\omega_0$ and close to $\phi \approx \pi/2$ for resonant cases with $\omega_p \simeq 2\omega_0$. As a rule, we find that the model spectra depend little on the choice of ϕ with the notable exception of the even harmonics produced by s-polarized incident light (see Section VIIC). The important parameter to be adjusted is X_s. For relativistic intensities $a_0 \gtrsim 1$, X_s is limited by

$$X_s \cos \alpha < \frac{c}{2\omega_0} = \frac{\lambda_0}{4\pi} \approx 0.08\lambda_0, \tag{24}$$

since the maximum surface velocity $V = 2\omega_0 \cos\alpha \, X_s < c$; such amplitudes are actually reached, as one sees, e.g., in Fig. 6.

The question may be raised why we do not calculate $X(t)$. In fact, an equation of motion can be derived from Equation (13e). Setting $\beta_x = \dot{X}(t)/c$, $d_t \beta_x = \ddot{X}(t)/c$, and also neglecting $\beta_x \partial_t \mathbf{a} = \beta_x \mathbf{a}\omega_0 \cos \alpha$ relative to $c \partial_x \mathbf{a} \simeq \omega_p \mathbf{a}$, making use of Equation (16) and $\beta_x \omega_0 \ll \omega_p$, we obtain

$$\ddot{X}(t) - \frac{1}{\gamma}(1 - (\dot{X}(t)/c)^2)f(X) = C\frac{1}{\gamma^2}(\mathbf{a}^2(X,t)$$
$$- a_y(X,t)\tan\alpha), \tag{25}$$

where

$$C = \omega_p^2 d_s(1 - (\omega_0 \cos\alpha/\omega_p)^2),$$
$$\gamma \cos\alpha = \sqrt{\frac{1 + (\mathbf{a}\cos\alpha)^2 - a_y \sin 2\alpha}{1 - (\dot{X}(t)/c)^2}}.$$

The problem is related to the restoring force $f(X)$ which is

$$f(X) = \partial_x \varphi = -(\omega_p/c)^2/\cos\alpha \, X(t) \tag{26}$$

for $X > 0$ inside the plasma, but behaves differently for $X < 0$ on the vacuum side; for the model density (21), the plasma restoring force on the electron surface at X even vanishes. Looking at the laser-driven electron surfaces obtained in the PIC simulations, the asymmetry is apparent. In none of the cases shown in Section IV is the trajectory $X(t)$ of the critical surface really symmetric with respect to $X > 0$ and $X < 0$, even for normal incidence with a harmonic driving

force. Only a kinetic model, like the one used in the PIC simulations, can describe this situation satisfactorily. Rather than trying to include these complications in the hydrodynamic model, we restrict ourselves to ansatz (23) and somewhat more complicated ones.

Here, we use Equations (25) and (26) only to estimate the density dependence of the surface amplitude. In the nonrelativistic limit and for normal incidence, one obtains $X_s \propto d_s a_s^2 \simeq (2a_0^2/k_0)(\omega_0/\omega_p)^3$; it decreases with plasma density like $k_0 X_s \propto (n_c/n)^{3/2}$. For obtaining large X_s and high output of harmonics, one should use a plasma density with relatively low $n/n_c > 1$. In particular for the resonant case $2\omega_0 = \omega_p$, large amplitudes occur and generate high harmonic intensities.

A. The reflected light

The wave equation

$$\left(\partial_x^2 - \frac{1}{c^2}\partial_t^2\right)\mathbf{a}(x,t) = \left(\frac{\omega_p}{c}\right)^2 \mathbf{s}(x,t) \tag{27}$$

with the source $\mathbf{s}(x,t)$ given by Equation (15) has the solution

$$\mathbf{a}(x,t) = \left(\frac{\omega_p}{c}\right)^2 \int_{-\infty}^{\infty} dx' \int_{-\infty}^{\infty} dt' \, g(x-x',t-t')\mathbf{s}(x',t'). \tag{28}$$

Using the Green function $g(x,t) = -(c/2)\Theta(t - |x|/c)$ leads to

$$\mathbf{a}(x,t) = -\frac{\omega_p^2}{2c}\int_{-\infty}^{\infty} dx' \int_{-\infty}^{t-|x-x'|/c} dt' \, \mathbf{s}(x',t'). \tag{29}$$

Let us consider an observer at some point $x \ll 0$ outside the plasma. The scaled electric field at the observer's position $\mathbf{e}(x,t) = e\mathbf{E}(x,t)/(m\omega_0 c) = -(1/\omega_0)\partial_t \mathbf{a}(x,t)$ is then obtained from Equation (29) in the form

$$\mathbf{e}(x,t) = \frac{\omega_p}{2\omega_0}\int_{-\infty}^{\infty} \frac{dx'}{l_s}\mathbf{s}(x',t - |x-x'|/c), \qquad l_s = \frac{c}{\omega_p}. \tag{30}$$

Recalling that the source is sharply localized with a step at the surface and an almost exponential decay over the skin depth l_s, the integral can be approximated by

$$\mathbf{e}(x,t) \simeq \frac{\omega_p}{2\omega_0}\mathbf{s}(X(t_{\text{ret}}),t_{\text{ret}}), \tag{31}$$

where the source is now taken exactly at the surface X and at the retarded time

$$t_{\text{ret}} = t - X(t_{\text{ret}})/c + x/c. \tag{32}$$

Equation (31) holds for normal incidence; oblique incidence is treated in Section VIIC.

In order to obtain $\mathbf{e}(x,t)$, one has to solve Equation (32) for t_{ret}. Due to the changing distance that the light has to travel between surface and observer, the observer sees the surface moving according to $\hat{X}(t) := X(t_{\text{ret}})$. Even if $X(t)$ oscillates harmonically, an anharmonic oscillation $\hat{X}(t)$ is observed. This is illustrated in Fig. 14. The thin solid line represents $X(t)$ according to Equation (23), choosing the am-
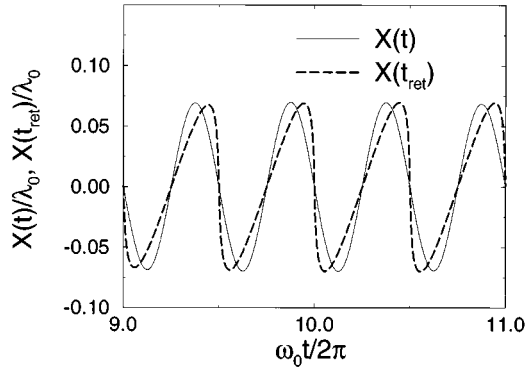
FIG. 14. Trajectory $X(t)$ of electron surface (solid line) and retarded surface trajectory $\hat{X}(t) = X(t_{\text{ret}})$ (dashed line) as seen by observer versus time; for parameters see the text.

FIG. 15. Comparison of PIC spectrum, obtained for parameters: $a_0 = 0.1$, $n_0/n_c = 4$, $\alpha = 0$, linear polarization. Model spectra are based on $X(t) = -0.007\lambda_0 \cos(2\omega_0 t - \pi/2)$ (adjusted to third harmonic) for different approximations for $X(t_{\text{ret}})$ marked by symbols.

plitude $X_s = 0.07\lambda_0$ close to the upper limit (24) and $\phi = \pi/2$; the broken line representing $\hat{X}(t)$ is obtained from

$$\hat{X}(t) = -X_s \sin(2\omega_0 t - 2k_0\hat{X}(t)) \tag{33}$$

with $k_0 = \omega_0/c$. Here and in the following, the observer's position is set to $x = x_{\text{obs}} = -\lambda_0$, for convenience. A simple way to solve Equation (33) is by iteration. The maxima of $\hat{X}(t)$ are shifted relative to $X(t)$ by $\Delta t = X_s/c$. As it turns out, it is this distortion due to retardation which is a major mechanism to generate the harmonics beside relativistic effects.

B. Harmonics at normal incidence

Using expression (15) for the source with $\alpha = 0$, the electric field is

$$\mathbf{e}(x,t) = \frac{1}{2}\frac{\omega_p}{\omega_0}\sqrt{1-(\dot{X}(t_{\text{ret}})/c)^2}\frac{\mathbf{a}(X(t_{\text{ret}}),t_{\text{ret}})}{\sqrt{1+\mathbf{a}^2(X(t_{\text{ret}}),t_{\text{ret}})}}, \tag{34}$$

where the driving field is

$$\mathbf{a}(X(t_{\text{ret}}),t_{\text{ret}}) = (2\omega_0\mathbf{a}_0 P(t_{\text{ret}})/\omega_p)\sin(\omega_0 t - \hat{X}(t)/c) \tag{35}$$

according to Equations (16), (17) and (22).

For a given laser pulse and plasma density, harmonics can now be calculated from Equation (34), and comparisons with PIC spectra are given in Figs. 3, 5 and 7. The function $P(t)$, defined in Section IV, is used to shape the envelope of the incident field ($\mathbf{a}_0 P(t)$) as in the PIC simulation; also, the surface motion $X(t)$ is switched on and off by this function. Almost perfect agreement is obtained, after adjusting just one parameter X_s. The adjusted amplitudes are somewhat smaller than the amplitudes of the critical surface observed in the density plots Figs. 2, 4 and 6, respectively. The phase of the surface oscillation [see Equation (23)] was set to $\phi = 0$ for the non-resonant case and to $\phi = \pi/2$ for the two resonant cases.
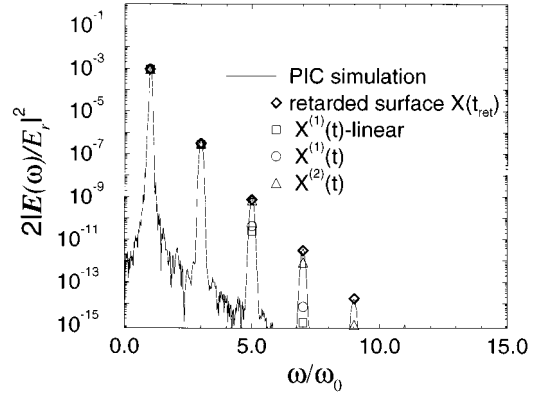
It is instructive to derive the model spectrum also analytically in lowest order of the driving field, valid for $a_0 \ll 1$. Dropping all relativistic square roots in Equation (34), one has

$$\mathbf{e}(x,t) = \frac{1}{2}\frac{\omega_p}{\omega_0}\mathbf{a}(t_{\text{ret}}) = P(t_{\text{ret}})\mathbf{a}_0 \sin(\omega_0 t + k_0 x - \omega_0\hat{X}(t)/c). \tag{36}$$

Neglecting surface motion, $\hat{X}^{(0)}(t) = 0$, this represents reflection without harmonics. Taking $\hat{X}^{(1)}(t) = -X_s\sin(2\omega_0 t)$ for resonant surface excitation ($\phi = \pi/2$) in first order approximation, one obtains

$$\mathbf{e}(x_{\text{obs}},t) = \mathbf{a}_0 \sin(\omega_0 t + \epsilon \sin(2\omega_0 t)), \tag{37}$$

with $\epsilon = k_0 X_s$, $k_0 x_{\text{obs}} = -2\pi$ and setting $P(t) \equiv 1$. Fourier expansion of Equation (37) gives

$$e(x_{\text{obs}},t)/a_0 = \sum_{n=0}^{\infty}(J_{2n}(\epsilon)+J_{2n+1}(\epsilon))\sin((4n+1)\omega_0 t),$$

$$+ \sum_{n=1}^{\infty}(J_{2n-1}(\epsilon)-J_{2n}(\epsilon))\sin((4n-1)\omega_0 t),$$

$$\simeq \sum_{n=0}^{\infty} J_n(\epsilon)\sin((2n+1)\omega_0 t), \tag{38}$$

where J_n denotes Bessel functions of first kind. The simplifying last step in Equation (38) is justified, since $\epsilon \ll 1$. In this approximation, the amplitude of the $(2n+1)$th harmonic is $J_n(\epsilon) \propto (\epsilon/2)^n/n!$ and decays faster than exponentially with order n. A comparison with a corresponding PIC simulation is given in Fig. 15 for $n_0/n_c = 4$ and $a_0 = 0.1$, again adjusting X_s and setting $\phi = \pi/2$. The approximation $\hat{X}^{(1)}(t) = -X_s \sin(2\omega_0 t)$ inserted into Equation (36) is represented by squares. Even though X_s is small in this case, less than one percent of the laser wavelength, one finds that only the third harmonic is described correctly and that the higher harmonics come out too low in this approximation. The circles and triangles denote the first $\hat{X}^{(1)}(t)$ and second $\hat{X}^{(2)}(t)$ it-

eration of Equation (33), respectively, taking also the square roots in Equation (34) into account. However, only the exact solution of Equation (33) reproduces the PIC results up to the highest harmonics. This means it is essential to take full account of retardation to find agreement with the PIC results.

C. Harmonics at oblique incidence

Let us finally extend the model to oblique incidence. Equation (30) then reads

$$\mathbf{e}(x,t)=\frac{\omega_p}{2\omega_0}\left[\int_{\hat{X}(t)}^{\infty}\frac{dx'}{l_s}\frac{\sqrt{1-\beta_x^2}(\mathbf{a}-\hat{\mathbf{y}}\tan\alpha)}{\sqrt{1+(\mathbf{a}\,\cos\alpha)^2-a_y\,\sin 2\alpha}}\right.$$

$$+\int_0^{\infty}\frac{dx'}{l_s}\hat{\mathbf{y}}\tan\alpha\bigg]$$

$$=\frac{\omega_p}{2\omega_0}\left[\int_{\hat{X}(t)}^{\infty}\frac{dx'}{l_s}\left(\frac{\sqrt{1-\beta_x^2}(\mathbf{a}-\hat{\mathbf{y}}\tan\alpha)}{\sqrt{1+(\mathbf{a}\,\cos\alpha)^2-a_y\,\sin 2\alpha}}\right.\right.$$

$$\left.+\hat{\mathbf{y}}\tan\alpha\right)+\hat{\mathbf{y}}\frac{\hat{X}(t)}{l_s}\tan\alpha\bigg],$$

where $\mathbf{a}=\mathbf{a}(x',t-|x-x'|/c)$. Taking the integral in the skin region leads to the approximate result

$$e_y(x,t)=\frac{\omega_p}{2\omega_0}\left[\frac{\sqrt{1-(\dot{\hat{X}}(t)/c)^2}(a_y(\hat{X}(t),t_{\text{ret}})-\tan\alpha)}{\sqrt{1+(\mathbf{a}(\hat{X}(t),t_{\text{ret}})\cos\alpha)^2-a_y(\hat{X}(t),t_{\text{ret}})\sin 2\alpha}}+\tan\,\alpha\left(1+\frac{\hat{X}(t)}{l_s}\right)\right], \quad (39)$$

$$e_z(x,t)=\frac{\omega_p}{2\omega_0}\frac{\sqrt{1-(\dot{\hat{X}}(t)/c)^2}a_z(\hat{X}(t),t_{\text{ret}})}{\sqrt{1+(\mathbf{a}(\hat{X}(t),t_{\text{ret}})\cos\alpha)^2-a_y(\hat{X}(t),t_{\text{ret}})\sin 2\alpha}}. \quad (40)$$

The additional term $\propto\hat{\mathbf{y}}\tan\alpha$, arising for oblique incidence, leads to a component $e_y(x,t)=(\omega_p/2\omega_0)\tan\alpha\,\hat{X}(t)/l_s$ in the radiated field proportional to the oscillation amplitude X. It would occur even for the case of vanishing incident field, provided the oscillation could be stimulated by some other mechanism. For oblique incidence, the electron oscillation in frame M appears as a wave running along the surface in frame L which radiates itself. For s-polarized incident light at non-relativistic intensity, it represents the only source for the second harmonic. Within the present model, however, this mechanism strongly overestimates the second harmonic and also the other even harmonics, as we see from the comparison with the PIC results in Fig. 8. We have checked that changing the phase ϕ does not improve the situation. The

failure may be related to the assumption (21) of a step-like electron density for the moving mirror; the PIC density profile is much softer in most cases. Suppressing the emission of the density wave by using Equations. (39) and (40) for s-polarized incident light and setting $a_y=-\tan\alpha\,\hat{X}(t)/l_s$ in addition to a_z, one would obtain the model spectrum marked by crosses in Fig. 9 which nicely reproduces the PIC spectrum. However, we have no clear understanding of this modification at the moment and feel that the model needs further refinement to describe the even harmonics satisfactorily.

Let us finally discuss extreme cases with $a_0=3$ far above the relativistic threshold. Density plots and corresponding spectra are shown in Figs. 16–19 for both s- and p-polarized pulses, incident with $\alpha=30°$ on a highly over-

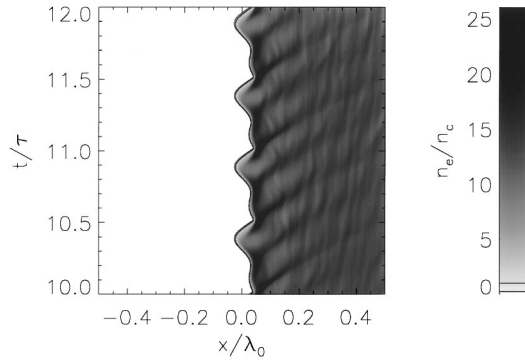FIG. 16. Electron density for oblique incidence of an s-polarized pulse with parameters: $a_0=3$, $n_0/n_c=13$, $\alpha=30°$. The pulse shape is the same as before (see Fig. 2), but with a 10τ plateau at peak intensity between the rising and falling parts. The contour lines mark the critical density $n=n_c$ and $n=0.2n_c$, respectively. The lower contour $n=0.2n_c$ is chosen instead of $n=0.1n_c$, since the latter corresponds to less than one particle per cell.
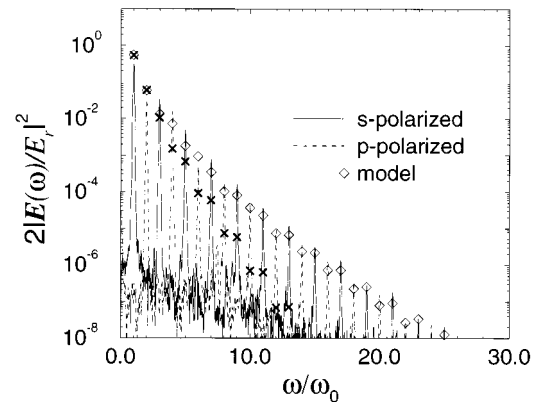

FIG. 17. Spectrum corresponding to the case of Fig. 16; diamonds refer to $X(t)=-0.021\lambda_0\cos(2(\omega_0\cos\alpha)t-\pi/3)-0.009\lambda_0\cos(4(\omega_0\cos\alpha)t-\pi/6)$ and the crosses to the same $X(t)$ except for dropping the $(4\omega_0)$ component.
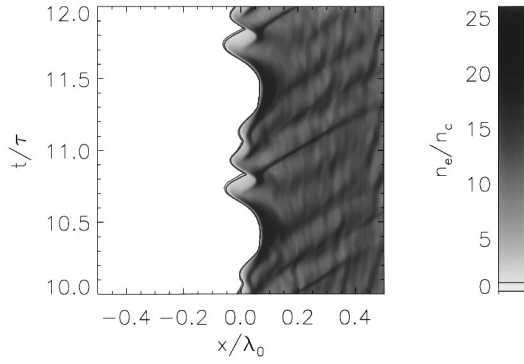
Phys. Plasmas, Vol. 3, No. 9, September 1996

Lichters, Meyer-ter-Vehn, and Pukhov   3435

FIG. 18. Electron density for oblique incidence of a *p*-polarized pulse with parameters: $a_0 = 3$, $n_0/n_c = 13$, $\alpha = 30°$, and same pulse shape as in Fig. 16. The contour lines mark the critical density $n = n_c$ and $n = 0.2n_c$, respectively.
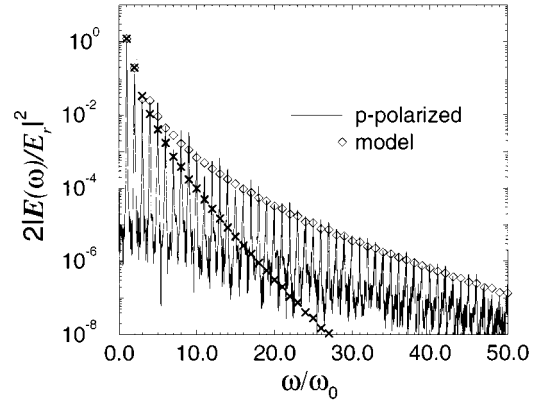

FIG. 19. Spectrum corresponding to the case of Fig. 18; diamonds refer to the model with $X(t)/\lambda_0 = 0.05 \sin((\omega_0 \cos\alpha)t) - 0.03 \cos(2(\omega_0 \cos\alpha)t) - 0.008 \cos(4(\omega_0 \cos\alpha)t)$ and the crosses to the same $X(t)$ except for dropping the $(4\omega_0)$ component.

dense plasma with $n_0/n_c = 13$. First notice the sharp surfaces obtained from the PIC simulations under these high irradiances; the $n/n_c = 0.2$ contour almost coincides with the $n/n_c = 1$ contour for both *s*- and *p*-polarization. The surface trajectories, on the other hand, differ considerably. For *p*-polarization, the fundamental period is τ, whereas it is $\tau/2$ for *s*-polarization, since the ω_0 driving mode is absent and the $2\omega_0$ mode of the ponderomotive force is leading. However, it is evident from Figs. 16 and 18 that there are additional modes present of order $4\omega_0$ and higher. These originate from the relativistic kinematics and correspond to the β- and γ-factors in the equation of motion (25).

The corresponding spectra are given in Figs. 17 and 19. High harmonics are obtained, more for *p*-polarization in agreement with the larger surface amplitudes. They satisfy the general selection rules. These results confirm those of Gibbon.[18] The model results are marked in the spectra by the symbols. They are calculated from Equations (39) and (40). The surface trajectories $X(t)$ are represented by a few modes which roughly reproduce the surface motion shown in the corresponding density plots. Omitting the relativistic $4\omega_0$ mode in the surface motion, the crosses are obtained which clearly miss the PIC results. When adding the $4\omega_0$ mode, one can well reproduce the spectrum for *p*-polarization. Also, fair overall agreement is found for the *s*-polarized case; in this case, the relative intensity of odd and even harmonics turns out to be sensitive to the relative phase ϕ between the driving field and the $2\omega_0$ surface mode, and the results shown in Fig. 17 correspond to $\phi = 60°$. We conclude that the oscillating mirror model works also for highly relativistic intensities.

VIII. SUMMARY AND CONCLUSIONS

In summary, we have presented PIC simulations showing harmonic generation from steplike density profiles at normal and oblique incidence of *s*- and *p*-polarized light. The yield of high harmonics strongly increases when approaching and exceeding the relativistic threshold intensity $I\lambda_0^2 \simeq 10^{18}$ W cm$^{-2}\mu$m^2. The harmonic output also increases with decreasing plasma density and is particularly large for $\omega_p = 2\omega_0$, when the oscillating part of the ponderomotive

force is at resonance with the plasma frequency. For *s*-polarized incident light, the output decreases monotonically with α. For *p*-polarized incident light, an optimal angle exists because of the combined action of the ponderomotive force and the normal component of the electric field of the pulse. This angle depends on incident intensity and plasma density; for example, we find $\alpha \simeq 30°$ for $a_0 = 0.5$ and $n_0/n_c = 4$.

A set of relativistic cold plasma fluid equations has been newly derived here for oblique incidence. It is used to interpret the PIC results. In particular, the following selection rules are derived: (1) *s*-polarized incident light generates *s*-polarized odd harmonics and *p*-polarized even harmonics; (2) *p*-polarized incident light generates *p*-polarized odd and even harmonics, but no *s*-polarized reflected light; (3) circularly polarized light at normal incidence produces no harmonics at all. These selection rules are valid under the condition of planar symmetry and may be violated in experiments due to spatial distortions.

Another important conclusion of this paper concerns the mechanism of harmonic generation at steep boundaries. The PIC simulations show that the laser excites strong oscillations of the electron density surface, forming a moving mirror. The harmonics can be understood to a large extent in terms of laser reflection from this mirror, when taking proper account of retardation and relativistic effects. This model allows us to reproduce the PIC spectra almost quantitatively. Low plasma density (yet overdense) enables large amplitudes of the surface motion which leads to enhanced harmonic output.

Another option for soft boundaries are ablation layers with longer scale lengths as they occur in traditional laser plasma physics with longer pulses. The high yield of harmonics obtained with nanosecond CO_2 lasers pulses[6–8] can be interpreted in this way. In short-pulse laser experiments, prepulses may do the job. The recent results by Norreys *et al.*,[5] showing harmonics up to the 68th with picosecond 10^{19} W/cm^2 pulses, point in this direction. Since varying the scale length of the initial plasma surface introduces a whole new dimension, a corresponding systematic investigation is left for a separate publication.

Lichters, Meyer-ter-Vehn, and Pukhov

ACKNOWLEDGMENTS

[1] M.D. Perry and G. Mourou, Science **264**, 917 (1994).

[2] A. L'Huillier, K.L. Schafer, and K.C. Kulander, J. Phys. B **24**, 3315 (1991).

[3] S. Kohlweyer, G.D. Tsakiris, C.-G. Wahlström, C. Tillman, and I. Mercer, Opt. Commun. **117**, 431 (1995).

[4] D. von der Linde, T. Engers, G. Jenke, P. Agostini, G. Grillon, E. Nibbering, A. Mysyrowitz, and A. Antonetti, Phys. Rev. A **52**, R 25 (1995).

[5] P.A. Norreys, M. Zepf, S. Moustaizis, A.P. Fews, J. Zhang, P. Lee, M. Bakarezos, C.N. Danson, A. Dyson, P. Gibbon, P. Loukakos, D. Neely, F.N. Walsh, J.S. Wark, and A.E. Dangor, Phys. Rev. Lett. **76**, 1832 (1996).

[6] R.L. Carman, C.K. Rhodes, and R.F. Benjamin, Phys. Rev. A **24**, 2649 (1981).

[7] R.L. Carman, D.W. Forslund, and J.M. Kindel, Phys. Rev. Lett. **46**, 29 (1981).

[8] B. Bezzerides, R.D. Jones, and D.W. Forslund, Phys. Rev. Lett. **49**, 202 (1982).

[9] C. Grebogi, V. Tripathi, and H. Chen, Phys. Fluids **26**, 1904 (1983).

[10] S.C. Wilks, W.L. Kruer, M. Tabak, and A.B. Langdon, Phys. Rev. Lett. **69**, 1383 (1992).

[11] A. Pukhov and J. Meyer-ter-Vehn, in *Proceedings, International Conference on Laser Interaction and Related Plasma Phenomena*, Osaka, April 1995, edited by K. Nishihara, Institute of Laser Engineering, AIP Conference Proceedings (American Institute of Physics, Woodbury, NY, in press).

[12] A. Bourdier, Phys. Fluids **26**, 1804 (1983).

[13] S.C. Wilks, W.L. Kruer, and W.B. Mori, IEEE Trans. Plasma Sci. **PS-21**, 120 (1993).

[14] A. Bergmann and P. Mulser, Phys. Rev. E **47**, 3585 (1993); H. Ruhl and P. Mulser, Phys. Lett. A **205**, 388 (1995).

[15] P. Gibbon and A.R. Bell, Phys. Rev. Lett. **68**, 1535 (1992).

[16] P. Gibbon, Phys. Rev. Lett. **73**, 664 (1994).

[17] S.V. Bulanov, N.M. Naumova, and F. Pegoraro, Phys. Plasmas **1**, 745 (1994).

[18] P. Gibbon, Phys. Rev. Lett. **76**, 50 (1996).

[19] P. Sprangle, E. Esarey, and A. Ting, Phys. Rev. A **41**, 4463 (1990).

[20] C.K. Birdsall and A.B. Langdon, *Plasma Physics via Computer Simulation,* Series on Plasma Physics (Adam Hilger, New York, 1991).

[21] F. Brunel, Phys. Rev. Lett. **59**, 52 (1987).

[22] D. von der Linde, H. Schulz, T. Engers, and H. Schüler, IEEE J. Quantum Electron. **QE-28**, 2388 (1992).